Analysis *in vivo* using a new method, ARGO (Analysis of Red Green Offset), reveals complexity and cell-type specificity in presynaptic turnover of synaptic vesicle protein Synaptogyrin/SNG-1

Nikita Shiliaev[1], Sophie Baumberger[1], and Claire E. Richardson[1]*

[1]Department of Genetics, University of Wisconsin-Madison
425 Henry Mall, Madison, WI, 53706-1580 USA

*Corresponding author: claire.richardson@wisc.edu

Running Head: Synaptic vesicle protein SNG-1 turnover

Abstract

In long-lived cells such as neurons, proteostasis involves the regulated degradation and replacement of proteins to ensure their quality and appropriate abundance. Synaptic vesicle (SV) protein turnover in neurons is important for controlling the SV pool size to maintain appropriate levels of neurotransmission; yet, it is incompletely understood, partly due to limited tools for quantifying protein turnover in vivo. We present ARGO (Analysis of Red-Green Offset), a fully genetically encoded, ratiometric fluorescence imaging method that visualizes and quantifies protein turnover with subcellular resolution in vivo. ARGO is inexpensive, modular, and scalable for use in genetically tractable experimental organisms. Using ARGO, we examine the turnover of Synaptogyrin/SNG-1, an evolutionarily conserved, integral SV protein, in *C. elegans* neurons. We show that the SNG-1 turnover rate is consistent across presynapses within a single neuron but varies between neuron classes. Notably, we find SNG-1 and can exist in two distinct, non-intermixing populations within each presynapse. Further, we present an initial mutant analysis of *uba-1*, the sole E1 ubiquitin ligase in *C. elegans*, showing that we can detect slowed SNG-1 turnover even though steady-state SNG-1 abundance is not increased compared to wild-type. These results provide new hints for the regulation of SV pool size.

Significance Statement

- In long-lived cells, a protein's rates of synthesis and degradation together determine its abundance, yet regulation of protein turnover is largely unknown due to the lack of simple methods for in vivo quantification.
- Using *C. elegans*, the authors develop ARGO, a genetically encoded, microscopy approach that quantifies a protein's turnover. Results suggest that synaptic vesicle protein Synaptogyrin/SNG-1 can partition into two presynaptic pools with distinct half-lives.
- This provides a powerful tool to study protein turnover, reveals an unexpected complexity in SNG-1 turnover, and lays the groundwork for future investigations of synaptic vesicle protein compartmentalization, sorting, and degradation.

Introduction

For neurons and other long-lived cells, maintenance of cellular function requires maintenance of proteostasis. Part of proteostasis is the continuous turnover and replacement of most proteins, which is proposed to generate multiple benefits; these include promoting stability in protein levels despite

stochastic variations and errors in gene expression, removing damaged proteins, and minimizing accumulation of protein damage, and regulating protein abundance (Reddien, 2024). The importance of this continuous turnover is highlighted by the consequence of its failure: declining proteostasis, including the accumulation of misfolded and damaged proteins, is a hallmark of aging and a central driver of neurodegenerative disease (Hipp *et al.*, 2019; López-Otín *et al.*, 2023). Neurons' complex morphology presents a spatial challenge for turnover of synaptic proteins, as most protein degradation machinery resides in the neuron cell body (Winckler *et al.*, 2018). However, homeostatic protein degradation remains incompletely understood for most proteins in any cell type. An obstacle to understanding this is the lack of easy and robust methods to interrogate protein half-life *in vivo* with high spatial and temporal resolution.

Several methods can be used to quantify homeostatic protein turnover. Pulse-chase labeling with heavy-isotope-containing amino acids followed by bulk proteomics to measure reduction in labeled protein over time has the strength of simultaneously measuring the half-life of thousands of proteins (Zhou, 2004). This method is laborious, though, especially *in vivo,* and the ability to measure protein half-life with cellular or subcellular resolution is limited since all of an animal's cells are labeled. Fluorescence microscopy-based approaches enable assessment of an individual protein-of-interest's turnover with high resolution. This has been achieved using photoconvertible fluorescent proteins, which requires calibration of the photoconversion to minimize phototoxicity in the pulse (Zhang *et al.*, 2007). Another strategy is to label the protein-of-interest with a self-labeling tag, most commonly SNAP-tag or HaloTag, provide a "pulse" of fluorescent ligand, then image turnover with fluorescence microscopy during the "chase" (Bojkowska *et al.*, 2011). Such experiments contributed evidence that, in cultured hippocampal neurons, SV proteins function in SV cycling for less than half of their total half-life, and, once decommissioned from SV cycling, they continue to reside at presynapse (Truckenbrodt *et al.*, 2018). Considering those results, one might speculate that the management of SV protein turnover as a whole, including the sorting out of the functional pool, is especially stringent Recently, this method was used to visualize and quantify the homeostatic degradation of post-synaptic protein PSD95 in the mouse brain using PSD95-HaloTag (Bulovaite *et al.*, 2022). This was the first time homeostatic protein degradation of any neuronal protein has been quantified with notable spatial resolution *in vivo*, and the results indicated that PSD95 turnover depends on animal age, region of the brain, and subcellular region within individual neurons (Bulovaite *et al.*, 2022). Such variation is consistent with the notion that synaptic protein turnover is highly regulated and may play in important role in specifying differences in synaptic function across different neuron types.

Importantly, comparing protein half-life between multiple separate studies that used the heavy-isotope-pulse-plus-proteomics approach shows that cultured neurons have dramatically shorter protein

half-lives overall than neurons *in vivo* (Price *et al.*, 2010; Cohen *et al.*, 2013; Visscher *et al.*, 2016; Dörrbaum *et al.*, 2018; Fornasiero *et al.*, 2018; Heo *et al.*, 2018; Mathieson *et al.*, 2018; Kluever *et al.*, 2022). This indicates that there is a difference in the regulation of protein degradation in an adult animal's functioning nervous system versus in immature, cultured neurons. This could be due to a variety of factors, including neuron age, neuron morphology, or cell-extrinsic environment; nevertheless, it highlights the value of studying protein turnover *in vivo*.

Here, we developed a new method to visualize the turnover of a protein of interest with high spatial and temporal resolution *in vivo* using fluorescence microscopy. We call this method ARGO (Analysis of Red Green Offset), drawing an analogy to the Theseus Ship Paradox, which ponders how identity persists even as components are gradually replaced over time. This method could, in theory, be applied to any protein-of-interest for which addition of a fluorescent tag does not impact localization or function.

We used ARGO to begin to directly analyze the turnover of SV proteins in adult neurons *in vivo.* SV proteins of are particular interest because the abundance, composition, and functionality of SV pools at each presynapse contributes to determining the amount of neurotransmission. Furthermore, measuring their turnover provides an opportunity to test whether SV pools are maintained as spatially or functionally distinct compartments within individual neurons, as non-uniform intracellular turnover would imply such distinctions. We chose Synaptogyrin/SNG-1 as our first protein of interest because it is an evolutionarily conserved transmembrane SV protein, it is present on most SVs, and it regulates SV cycling (Abraham *et al.*, 2011; Raja *et al.*, 2019). These features make SNG-1 an informative starting point for establishing ARGO and for probing principles of SV protein turnover. As it is an integral membrane protein, it is expected to be degraded via endosomal sorting to lysosomal compartments.

Indeed, prior research mainly using assessment of steady-state SV protein localization combined with genetic analyses has led to the model that SV proteins are sorted into late endosomes and/or autophagosomes at the synapse, then transported to the cell body for degradation within lysosomal compartments (Uytterhoeven et al. 2011; Fernandes et al. 2014; Sheehan et al. 2016; Okerlund et al. 2017). Interestingly, though, an imaging strategy to assess steady-state SV protein degradation during brain development in *D. melanogaster* found evidence that at least some SV protein is degraded in an axonal degradative "hub" (Jin *et al.*, 2018). Another aspect under investigation is how the rate of SV protein degradation is regulated, with evidence pointing to both surveillance and/or sorting for degradation as rate-limiting steps (Fernandes *et al.*, 2014; Sheehan *et al.*, 2016; Okerlund *et al.*, 2017; Sheehan and Waites, 2019; Hoffmann-Conaway *et al.*, 2020; Birdsall *et al.*, 2022). A more direct observation of SV protein turnover will potentiate a deeper understanding of this process.

132

133 # Results

134 ## Strategy and validation of SNG-1::ARGO

135 To enable the analysis of protein turnover with subcellular resolution *in vivo*, we developed the
136 ARGO (Analysis of Red Green Offset) method (Figure 1A). The ARGO construct cell-specifically, co-
137 translationally labels the protein-of-interest with both RFP and GFP in a tandem tag. Cell specificity is
138 achieved using FLP/FRT, wherein the Flippase is expressed from cell-specific promoters. The steady-
139 state GFP/RFP ratio of an ARGO-tagged protein reflects the mechanism of degradation. As GFP
140 fluorescence is quenched in acidic environments, ARGO-tagged proteins that have been sorted for
141 degradation within lysosomal compartments are detected as endosomes with stronger RFP than GFP
142 fluorescence (Figure 1B). Alternatively, the absence of detectable lysosomal compartments suggests
143 that the protein-of-interest is degraded by the proteasome, or not at all. Next, the ARGO "pulse" removes
144 *gfp* from the *argo* gene cassette such that all newly produced molecules of the protein-of-interest are
145 labeled with only RFP. The neuron is then periodically imaged with fluorescence confocal microscopy,
146 and the GFP/RFP ratio is quantified for each fluorescent punctum throughout the cell to determine the
147 proportion of "old" versus "total" protein-of-interest both spatially and temporally.

148 To study SV protein turnover, the *argo* cassette was inserted into the *sng-1* genomic locus such
149 that the RFP::GFP tandem tag will be attached to the C-terminus of SNG-1, which resides on the
150 cytoplasmic side of SVs (Figure 1A). Expression of Flippase from a pan-neuronal reporter shows SNG-
151 1::ARGO dually labeled with RFP and GFP fluorescence throughout the nervous system (Figure 1C).
152 Driving Flippase expression from neuron-specific promoters, we turned on SNG-1::ARGO expression in
153 three individual neuron classes that represent a variety of morphologies and functions: the cholinergic
154 motor neuron DA9, the two bilaterally symmetric serotonergic NSM neurons, and the GABAergic motor
155 neurons VD/DD (Figures 1D-F). Each of these neuron types elaborates multiple *en passant* synapses
156 that can be visualized as individual puncta using fluorescence confocal microscopy (White *et al.*, 1986).
157 The use of neuron-specific Flippase transgenes enables visualization of these individual presynapses, to
158 which SNG-1::ARGO localizes as expected, with co-localized fluorescence from RFP and GFP (Figures
159 1D-F)(Schwartz and Jorgensen, 2016; Muñoz-Jiménez *et al.*, 2017). In the absence of Flippase, no
160 fluorescence is observed from the *sng-1::argo* allele (Figure 1G).

161 For the ARGO method to provide meaningful information about protein turnover, it must not
162 impact the function of the protein-of-interest. This is because each of the facets of a protein's function,
163 including folding, localization, and activity, are factors that could be inputs to regulate its turnover. For
164 SNG-1::ARGO, proper localization to the presynapses is the first indicator that this allele is usable. Next,
165 we assessed *sng-1* function. Synaptogyrin/SNG-1 regulates synaptic transmission from worms to

166 mammals (Abraham *et al.*, 2011; Raja *et al.*, 2019). In *C. elegans*, loss of *sng-1* function causes
167 resistance to the acetylcholinesterase inhibitor aldicarb, suggesting that the *sng-1(o)* mutant has reduced
168 SV release compared to wild-type (Figure 1H)(Mahoney *et al.*, 2006; Abraham *et al.*, 2011). By contrast,
169 pan-neuronally expressed SNG-1::ARGO has no discernable effect on aldicarb resistance (Figure 1H),
170 suggesting that the SNG-1::ARGO protein is functional. Together, these results suggest that SNG-
171 1::ARGO is likely a valid tool for investigating SNG-1 biology.
172 To generate the pulse that activates ARGO, we excised *gfp* from the *ARGO* gene cassette using
173 a heat-shock promoter to drive production of Cre recombinase upon a brief heat shock. This is the
174 quickest and most robust method to induce gene expression in *C. elegans*. Indeed, by assessing
175 fluorescence in non-heat-shocked animals and in animals several days post-heat-shock, we observed
176 that this method efficiently activated SNG-1::ARGO in each of the three neuron types we examined, with
177 little ectopic excision of *gfp* in the absence of heat shock (Table 1, Figure S1A). Though it is practical, a
178 drawback to this approach is that heat shock causes increased production of HSF-1-regulated genes
179 including chaperones, which will impact proteostasis. To assess whether this is likely to have a
180 substantial impact on SNG-1 turnover dynamics or mechanisms, we assessed whether *sng-1* mRNA or
181 protein abundance are altered by the heat shock pulse. We reasoned that, if neither the rate of SNG-1
182 production nor the steady-state abundance of SNG-1 is impacted by the heat shock, then it is unlikely
183 that the degradation is altered. We observe no significant difference in *sng-1* mRNA levels either 5 hours
184 or 1 day after heat-shock (Figure S1B). To assess steady-state SNG-1 protein abundance, we quantified
185 average presynaptic SNG-1::ARGO RFP intensity and number of synapses in the DA9 neuron. There
186 was no significant difference 4 hours, 1 day, or 2 days after heat shock compared to control (Figure S1C-
187 D). We detect an increase in the presynaptic SNG-1::ARGO GFP/RFP ratio immediately following heat-
188 shock that is not detectable by 4 hours or 1 day post-heat shock (Figure S1E). That timing is expected to
189 be too fast to reflect a change in *sng-1* gene expression; it is therefore likely to reflect a change in
190 localization, such as decreased SV cycling or trafficking. Still, the difference is resolved by 4 hours post
191 heat-shock and that the first post-heat shock imaging timepoint used in turnover experiments is 1 day.
192 Together, these data indicate that SNG-1::ARGO turnover is unlikely to be substantially impacted by the
193 heat shock pulse. Concerns about a potential subtle impact are mitigated by the fact that all turnover
194 comparisons were made between cohorts that received the same heat shock.
195 Experimentally, the ARGO pulse is a 1-hour heat shock at 34 °C, but the pulse in terms of
196 generating a Time = 0 for turnover experiments requires production of Cre, Cre-mediated removal of the
197 *gfp* gene, and degradation of the mRNA molecules encoding *sng-1::rfp::gfp.* We assessed the effective
198 timing of the pulse by imaging presynapses 4 hours post-heat shock (Figure S1F-L). Whereas we detect
199 no change in SNG-1::ARGO GFP/RFP in a heat-shocked strain lacking the *HS>Cre* transgene, there

200 was a significant decrease in the GFP/RFP ratio in five of the six neuron-by-animal-age conditions tested
201 (Figure S1F-L). In addition, the abundance of Cre-recombined *sng-1::argo* alleles in the genome peaked
202 by 4 hours post-heat shock (Figure S1M). Therefore, the ARGO pulse effectively takes on the order of
203 several hours, and the ARGO method systematically over-estimates protein half-life by that much. For
204 comparison, the mean half-life of the *C. elegans* proteome is estimated to be on the order of a day or two
205 (Depuydt *et al.*, 2016; Visscher *et al.*, 2016).
206

207 **SNG-1 is likely sorted for degradation at the presynapse and degraded in the cell body**

208 Assessing steady-state SNG-1::ARGO, we observed that there are fluorescent puncta within the
209 neuron cell bodies that show relatively stronger RFP intensity compared to GFP intensity (Figure 1C-F).
210 Super-resolution microscopy resolved two distinct populations of SNG-1::ARGO-labeled endosome in
211 the neuron cell body: GFP-brighter endosomes, which are likely newly synthesized and trafficking
212 endosomes, and RFP-brighter endosomes, which are likely SNG-1 within acidic lysosomal
213 compartments (Figure 1I). Furthermore, transport packets of both the GFP-brighter and RFP-brighter
214 flavors are present along the proximal axon and commissure (Figure 1I). These data suggest that SNG-
215 1::ARGO is trafficked retrogradely from the presynapses to the cell body in acidified lysosomal
216 compartments for degradation (Figure 1I).

217 We measured the steady-state SNG-1::ARGO GFP/RFP ratio at each presynapse per neuron in
218 the DA9 neuron from Day 0 (L4 larval stage, A0) to Day 7 of adulthood (A7) (Figure 2A). For
219 comparison, mean adult lifespan is ~15 days (Gems and Riddle, 2000). Note that GFP has a higher
220 quantum yield than RFP and is consistently brighter *in vivo,* so a ratio greater than 1 was expected
221 (Rodriguez *et al.*, 2017). Indeed, mean presynaptic SNG-1::ARGO GFP/RFP ratio at A0 was >2 (Figure
222 2A). Mean presynaptic SNG-1::ARGO GFP/RFP declined between A0 to A2, then remained fairly stable,
223 with a trend for progressive slight decrease that was resolved at A7 (Figure 2A).

224 To better understand the change in ratio between A0 to A2, we examined the RFP and GFP
225 intensities underlying the ratiometric data (Figure 2B-C). *C. elegans* body size increases between A0
226 and A2, and the DA9 synapses likewise increase in both number and size based on the RFP intensity
227 (Figure S1D, 2B, 2D). The average steady-state (no pulse) SNG-1::ARGO GFP fluorescence intensity
228 per synapse likewise increases, but by only half as much, underlying the decrease in the presynaptic
229 SNG-1::ARGO GFP/RFP ratio (Figure 2C-D).

230 We hypothesized that A) SNG-1::ARGO is sorted into acidified compartments, likely late
231 endosomes, at the presynapse, which partially quenches the GFP fluorescence, and B) the steady-state
232 proportion of presynaptic SNG-1::ARGO that resides within acidified compartments increases in early
233 adulthood. To test this hypothesis, we injected mid-adult animals with Bafilomycin A, which inhibits the

234 V-ATPase that acidifies lysosomes and late endosomes. Indeed, animals injected with Bafilomycin A
235 showed an increase in the presynaptic SNG-1::ARGO GFP/RFP ratio 3 hours post-injection compared to
236 control and vehicle-injected animals (Figure 2E). Furthermore, we have shown that injecting animals with
237 concanamycin A, which also blocks the V-ATPase, increased the SNG-1::ARGO GFP/RFP ratio at both
238 the presynapse and the neuron soma within hours (Zhong and Richardson, 2025). Consistent with this
239 interpretation, late endosomes and autophagosomes, which both acquire acidified lumens, localize to
240 presynapses (Ceccarelli *et al.*, 1973; LaVail and LaVail, 1975; Grill *et al.*, 2007; Binotti *et al.*, 2014;
241 Soukup *et al.*, 2016; Stavoe *et al.*, 2016; Neisch *et al.*, 2017).
242 Taken together, these data suggest that SNG-1::ARGO is sorted for degradation into acidified
243 compartments at the presynapse and then trafficked to the cell body to complete degradation. This
244 aligns with the prevailing model for SV protein turnover, which was mainly based on more indirect
245 evidence including genetic analysis of steady-state abundance and the presence of MVBs and
246 autophagosomes at presynapses. Of note, SNG-1 within partially acidified compartments is not
247 necessarily destined for degradation; this notion is considered further below.
248 Next, we assessed whether presynaptic SNG-1::ARGO GFP/RFP ratio is dependent on
249 presynapse position. We binned the presynapses as “proximal,” “middle,” or “distal” along the axon and
250 compared the steady-state GFP/RFP for each day (Figure 2F). There was no consistent relationship
251 between synapse position and ratio (Figure 2F).
252
253 **Quantification of presynaptic SNG-1::ARGO turnover in the DA9 neuron**
254 Using the DA9 neuron, we pulsed SNG-1::ARGO at A2 and then imaged unique cohorts of
255 animals daily for five days afterward, plus a cohort immediately before and after the activation (Figure
256 3A-B, S1H). SNG-1::ARGO GFP/RFP ratios were normalized to the mean ratio from age-matched
257 control (non-pulsed) cohorts imaged in parallel. From A2, presynapse size (based on SNG-1::RFP
258 intensity) and presynapse number are fairly stable (Figure 2B, S1A,C,D), meaning that the SNG-1::RFP
259 level meaning that the declining SNG-1::ARGO GFP/RFP each day after the pulse is predominantly due
260 to homeostatic SNG-1 turnover. Fitting a single-phase exponential decay function to the data calculated
261 an apparent presynaptic half-life of 3.0 days (95% C.I. 2.7 - 3.4 days). We observed no impact of
262 presynapse position relative to the neuron cell body on the half-life (Figure 3C). To assess whether some
263 other feature of individual presynapses might regulate turnover rate within a neuron, we quantified the
264 intraneuronal coefficient of variation (CV) in presynaptic SNG-1::ARGO GFP/RFP for each timepoint in
265 the pulse-chase (Figure 3D). If the rate of SNG-1::ARGO turnover varies by presynapse, we expect to
266 observe an increase in CV during the chase, especially at timepoints close to the pan-synaptic half-life,
267 compared to T=0. However, no change in CV was detected.

268 We performed a pulse-chase experiment with the DA9 SNG-1::ARGO starting at A0. From A0 to
269 A2, the DA9 presynapses grow by over 100%, and additional presynapses are added, scaling with
270 increasing animal size (Figure 2B-D, S1D). The apparent presynaptic SNG-1::ARGO half-life – 1.7 days
271 (95% C.I. 1.5-1.9 days) – therefore measures a combination of both the removal of old molecules of
272 SNG-1 from synapses and the increasing total abundance of SNG-1 (Figure 3E). The shorter apparent
273 half-life with the pulse at A0 compared to A2 is likely due to this scaling as opposed to a change in the
274 rate of SNG-1 degradation. Indeed, fitting one-phase exponential decay curves to both the A2 and A0
275 datasets using the GFP intensity rather than the GFP/RFP ratio, we observe no difference in apparent
276 half-life between the two different pulse times (Figure S2A-B). With the pulse at A0, the calculated SNG-
277 1 half-life is longer using mean GFP, which only quantifies degradation, compared to using the GFP/RFP
278 ratio which quantifies degradation plus synapse growth. By contrast, with the pulse at A2, the half-life
279 calculated using mean GFP is indistinguishable from that calculated using the GFP/RFP ratio, though
280 the 95% C.I. is substantially larger. Indeed, using the GFP intensity instead of the GFP/RFP ratio to fit
281 the exponential decay function results in substantially lower R^2 values (>0.72 for ratiometric versus <0.29
282 for GFP only) and wider 95% C.I.s (<0.8 d for ratiometric versus >2.4 d for GFP only) for both
283 experiments (Figure 3B-D, S2A-B). This demonstrates the utility of incorporating ratiometric
284 quantification for turnover analysis.
285 Returning to the presynaptic scaling that occurs between A0 to A2, the SNG-1::ARGO pulse-
286 chase experiment affords an opportunity to assess whether newly synthesized SNG-1::ARGO, which is
287 tagged with only RFP, is allocated to the presynapses with any spatial pattern. Such a pattern could be
288 generated by synapse position or activity (i.e. the amount of SV cycling), and it could be detected as an
289 increase in the intraneuronal CV in presynaptic SNG-1::ARGO GFP/RFP ratio in the chase compared to
290 the pulse. No such increase was detected, indicating that newly synthesized SNG-1 is evenly distributed
291 throughout the neuron's presynapses (Figure 3F). This is consistent with the model that SV deposition at
292 both newly forming and fully formed presynapses strongly depends on trafficking parameters, and
293 continuous trafficking intermixes SVs between synapses (Staras *et al.*, 2010; Herzog *et al.*, 2011; Wu *et*
294 *al.*, 2013; Maeder *et al.*, 2014; Lipton *et al.*, 2018).
295
296 **SNG-1::ARGO turnover is slowed in a *uba-1*/E1 Ubiquitin ligase loss-of-function mutant**
297 As an initial mutant analysis using the ARGO method and a first step toward defining the
298 mechanisms of SNG-1 turnover, we constructed a strain carrying the DA9 *sng-1::argo* alleles and a
299 temperature-sensitive hypomorphic allele of *uba-1(it129ts),* which encodes the sole *C. elegans* E1
300 ubiquitin ligase (Kulkarni and Smith, 2008). Ubiquitination marks proteins for degradation via the
301 proteasome, the endolysosomal system, and some types of autophagy (Foot *et al.*, 2017; Yin *et al.*,

302 2020). Animals cultivated at the non-permissive temperature, 25 °C, looked fairly wild-type in terms of
303 presynaptic localization, organization, and number (Figure 3G-H), but they showed a reduction in
304 presynaptic SNG-1::ARGO RFP intensity, indicating that *uba-1* is required to promote retention and/or
305 delivery of SNG-1::ARGO to the presynapse (Figure 3I). In a turnover experiment with the pulse at A2,
306 the *uba-1(it129ts)* mutant showed a presynaptic SNG-1::ARGO half-life of 23.4 days (95% C.I. 7.8-
307 [upper limit could not be calculated])(Figure 3I, see also Figure S2C).
308 These data suggest that ubiquitination is likely required to promote SNG-1 degradation from the
309 presynapse. One hypothesis is that SNG-1 gets ubiquitinated and then sorted for degradation via
310 ESCRT; an alternate hypothesis is that SNG-1 turnover is regulated indirectly by ubiquitination of other
311 protein(s) in the neuron. Because the *uba-1(it129ts)* mutant is hypomorphic rather than amorphic, it is
312 possible that UBA-1 is essential for all presynaptic SNG-1 turnover. Of note, one might predict that a
313 reduction in homeostatic protein degradation could be revealed with steady-state imaging as an
314 increased abundance of the protein-of-interest; however, our results suggest that both presynaptic SNG-
315 1 removal and steady-state abundance decrease in the *uba-1(it129ts)* mutant, highlighting the utility of
316 quantifying turnover.
317
318 **Steady-state presynaptic SNG-1::ARGO varies with neuron identity**
319 We assessed steady-state presynaptic SNG-1::ARGO GFP/RFP in the NSM and VD2 neurons.
320 First, we compared the intraneuronal coefficient of variation across all presynaptic puncta of cohorts of
321 DA9, NSM, and VD2 neurons at A2. If any neuron type showed a notably higher interneuronal CV, it
322 could indicate that there is differential regulation in the sorting of SNG-1::ARGO into acidic
323 compartments within individual presynapses. However, the NSM interneuronal CV was similar to that of
324 DA9, and the CVs within VD2 neurons were low (Figure S2D).
325 We assessed steady-state SNG-1::ARGO across early adulthood and performed a turnover
326 experiment with the pulse at A2. The SNG-1::ARGO steady-state and turnover characteristics generally
327 were similar for NSM to those of the DA9 neuron (Figure S2D-J). The NSM neuron showed a stronger
328 steady-state position effect, though, with a trend that the more proximal synapses had a lower SNG-
329 1::ARGO GFP/RFP ratio compared to the more distal synapses (Figure S2H). Perhaps this is indicative
330 of an increased density of SNG-1-containing lysosomal compartments closer to the cell body, which
331 could arise due to SNG-1 retrograde trafficking in acidified compartments.
332
333 **Biphasic turnover of SNG-1::ARGO within each VD2 presynapse**
334 In the VD2 neuron with SNG-1::ARGO activation at A2, a one phase exponential decay curve
335 does not fit the data as well as it does for the DA9 and NSM neurons (VD2 $R^2 = 0.41$, DA9 $R^2 = 0.73$,

336 NSM R^2 = 0.63)(Figure 3B, 4A, S2I). A two-phase exponential decay curve fits the VD2 data better (R^2 =
337 0.48), and it is apparent that the curve plateaus above the calculated background (Figure 4A). Indeed,
338 according to the best-fit parameters for the two-phase curve, 39% of the SNG-1::ARGO molecules turn
339 over with a half-life of about 0.9 days, and the other 61% has essentially an infinite half-life (Figure 4A).
340 We considered whether this two-phase turnover could be due to non-specific or ineffective Cre-mediated
341 recombination specifically for the VD2 neuron, i.e., either some VD2 neurons would fail to recombine one
342 or both *gfp* alleles after the pulse and/or some VD2 neurons would recombine one or both alleles of *gfp*
343 during steady-state imaging. To assess this idea, we evaluated the interneuronal CV for each neuron-by-
344 age-by-treatment (Figure S3). If the VD2 neuron had inefficient and/or nonspecific removal of *gfp,* we
345 would expect to observe a higher CV in the VD2 neuron during the pulse-chase experiment and/or
346 steady-state imaging compared to the DA9 and NSM neurons. This trend was not observed (Figure S3).
347 As an alternate approach to assess whether the one-phase exponential decay curve can be ruled
348 out as a good descriptor of VD2 SNG-1::ARGO turnover, we fit a one-phase exponential decay curve to
349 the data with an unconstrained plateau. The best-fit plateau was significantly higher than the calculated
350 background, and the 95% C.I.s from the two calculations did not overlap (Figure 4B). By the same
351 analysis, the best-fit plateau and 95% C.I. for the NSM and DA9 neurons overlaps with that of the
352 calculated backgrounds (Figure 4B).
353 We assessed whether the two-phase curve in the VD2 neuron arose from distinct turnover
354 kinetics at spatially separate presynaptic puncta, i.e., some presynaptic puncta show turnover with a 0.9
355 day half-life while other presynaptic puncta within the same neuron show effectively no turnover. To do
356 this, we calculated the CV between all the presynaptic SNG-1::ARGO GFP/RFP ratios within each
357 neuron, across each timepoint of the turnover experiment (Figure 4C). We found no significant increase
358 in the average CV at any day post-activation compared to T=0 (Figure 4C). These data support the
359 model that each presynaptic punctum within an individual VD2 neuron exhibits the biphasic turnover.
360 We considered two models to explain the biphasic turnover in the VD2 presynapses. In Model 1,
361 there are two chronically distinct populations of SNG-1::ARGO within each presynapse, one with a
362 relatively fast turnover and the other with an unappreciable turnover. In Model 2, the mechanisms that
363 promote SNG-1 turnover are shut off or become dysfunctional as the animal ages, at an age that is
364 spanned by the turnover experiment. Model 1 predicts that the proportion of SNG-1 with an
365 unappreciable turnover will be the same regardless of animal age at which the SNG-1::ARGO is
366 activated (Figure 4D). By contrast, Model 2 predicts that the proportion of SNG-1 with an unappreciable
367 turnover will be lower when SNG-1::ARGO is activated in younger animals and higher when it is
368 activated in older animals (Figure 4D)(see Methods). To test these models, we performed an experiment
369 in which we activated the VD2 SNG-1::ARGO at A2 (versus A4 Day 2 and Day 4 of adulthood,

370 respectively) and imaged both groups at A7. The A2 group recapitulated the result from the full turnover
371 experiment, and the A4 group showed a similar amount of turnover as the A2 group, consistent with
372 Model 1 (Figure 4D). We also assessed the presynaptic GFP/RFP ratio in animals that were pulsed at
373 A2, then cultivated 25 °C instead of the standard 20 °C until imaging at A7. Animals age faster, have a
374 shorter lifespan, and exhibit compromised proteostasis at 25 °C; still, the presynaptic SNG-1::ARGO
375 GFP/RFP was about the same (Figure 4D); therefore, these results also align better with Model 1 than
376 Model 2.
377
378 **Evidence for endocytic sorting of SNG-1 in presynapse remodeling**
379 *C. elegans* has a series of GABAergic motor neurons with cell bodies along the ventral nerve
380 cord. A subset of these, called the VD neurons, make presynapses along the ventral nerve cord. In the
381 rest, called the DD neurons, presynapses are located along the dorsal nerve cord for most of the
382 animal's life. Quantifying SNG-1::ARGP GFP/RFP in the VD and DD neurons at different animal ages,
383 we found a strong age-by-neuron-identity interaction in regulating steady-state presynaptic SNG-
384 1::ARGO GFP/RFP (Figure 5). At the L2 larval stage, the VD neurons' mean ratio was 2.5, whereas the
385 DD neurons' mean ratio was less than 1.5 (Figure 5A-B). Presynapse size, based on the SNG-1::ARGO
386 RFP intensity, was similar in L2 larvae between the VD and DD neurons (Figure 5C). The DD neurons'
387 GFP intensity was low in L2 larvae, though (Figure 5D). We speculate that this difference between VD
388 and DD in L2 larvae is related to the distinct mechanisms of synaptic development between these two
389 otherwise similar classes of neuron. In the L1 larval stage, the DD neurons' presynapses are located
390 along the ventral nerve cord, and the VD neurons have not yet been generated. At the end of the L1
391 stage, the DD neurons' presynapses are relocated to the dorsal nerve cord (White *et al.*, 1978; Hallam
392 and Jin, 1998). This remodeling involves moving the pre-existing presynaptic proteins from the ventral to
393 the dorsal side (Park *et al.*, 2011). Meanwhile, the VD neurons are born, and they generate their initial
394 presynapses along the ventral nerve cord, where they remain. By imaging the VD/DD neurons in the L2
395 stage, we visualized the synapses shortly after this DD remodeling and VD synaptogenesis event. To fill
396 in the age gap between L2 and A2, we performed a separate experiment in which we assessed steady-
397 state SNG-1::ARGO in the VD versus DD neurons at L3 and A1 (Figure 5E-G). In both neuron classes,
398 the SNG-1::ARGO GFP/RFP ratio is significantly higher at L3 than at A1 (Figure 5E). Considering these
399 results together with the L2 versus A2 experiment suggests that the especially low SNG-1::ARGO ratio
400 in the DD neurons during or directly after presynapse remodeling is a transient condition, and the ratio
401 increases by the next larval stage.
402 Based on these results, we speculate that when SNG-1::ARGO in the DD neurons is relocated
403 from the ventral to the dorsal nerve cord, it is trafficked within acidified endosomes, wherein the GFP is

quenched. Both the SV-transporting kinesin KIF1A/UNC-104 and the more generalist Kinesin-1/UNC-116 are required for DD presynapse remodeling; consistent with our speculation, UNC-116 can transport endosomal and autophagic compartments (Klassen *et al.*, 2010; Park *et al.*, 2011; Kurup *et al.*, 2015; Stavoe *et al.*, 2016). In this speculation, the SNG-1::ARGO would be sorted out of the acidified compartments and into SVs in the newly formed DD dorsal presynapses.

Discussion

In summary, we developed and validated ARGO, a genetically encoded method to easily and inexpensively quantify protein turnover *in vivo* with high spatial and temporal resolution, and we used this method to begin to assess how transmembrane SV protein Synaptogyrin/SNG-1 is turned over from the presynapses in adulthood. These findings provide new insights into SV protein degradation, and they illustrate the utility of the ARGO method.

The ARGO method

The abundance of each of a cell's proteins is determined by its rates of production and degradation, plus the rate of cell division (Liu *et al.*, 2016). In terminally differentiated cells such as neurons, the protein degradation rate takes a more prominent role in controlling protein abundance (Liu *et al.*, 2016). Evidence from proteomic studies indicates that protein half-life can range from minutes to months (and, rarely, even longer), depending on the protein, the cell type, and the cellular context (Toyama *et al.*, 2013). An impediment to understanding the regulation of protein degradation is the limits of existing methods for easily assessing protein degradation *in vivo* with high resolution. The most straight-forward existing approach for interrogating a protein-of-interest's turnover is adding a self-labeling tag to that protein, most commonly SNAP-tag or HaloTag, providing a pulse of fluorescent ligand, then imaging turnover with fluorescence microscopy during the chase (Bojkowska et al. 2011; Bulovaite et al. 2022). ARGO is a conceptually and methodologically similar strategy with several advantages: First, because ARGO is fully genetically encoded, once the strain has been generated, performing experiments is simpler and cheaper. This makes it highly amenable to thorough interrogation of surveillance and degradation mechanisms, for example with forward and reverse genetics. Second, because the imaging is ratiometric, it provides higher resolution of protein half-life, and it is advantageous to use with genetic or circumstantial manipulations that alter the steady-state localization of the protein-of-interest. Third, because the GFP fluorescence is sensitive to acidic environments, analysis of steady-state fluorescence can determine whether and where degradation is mediated via

438 sorting into a lysosomal pathway. The design of ARGO is modular, making it amenable to modification.
439 For instance, though we used heat shock promoter to drive Cre expression here, any temporally
440 inducible transcription system can, in theory, be used to provide the pulse.
441

442 **SV protein degradation**

443 Our data indicate that SNG-1 is sorted for degradation at the synapse, then transported to the
444 cell body for degradation in lysosomal compartments. This corroborates the most prevailing, though
445 sometimes disputed, model for the spatial dynamics of SV protein degradation (Jin et al. 2018; Winckler
446 et al. 2018).

447 We found that the rate of SNG-1 turnover is similar across all the *en passant* presynapses within
448 a neuron regardless of their position relative to the cell body (Figure 3C, S2J). This contrasts with post-
449 synaptic protein PSD95, for which the turnover rate differs between post-synapses within a single neuron
450 based on their spatial positioning in the mouse brain (Bulovaite et al. 2022). Perhaps the continuous
451 trafficking of SVs between synapses generates the conditions in which SNG-1 functions as a single
452 super-pool in regard to turnover (Staras et al. 2010; Herzog et al. 2011; Wu et al. 2013). Alternatively,
453 the molecules and mechanisms that regulate the rate of SNG-1 degradation could be effectively uniform
454 across presynapses.

455 Our results indicate that reduction-of-function of the sole *C. elegans* E1 ubiquitin ligase, *uba-1*,
456 leads to reduced steady-state presynaptic SNG-1 abundance as well as dramatically slowed SNG-1
457 turnover from the presynapse. We have recently shown that loss of Transcription Factor EB/HLH-30
458 likewise causes reduced steady-state presynaptic SNG-1 abundance along with slowed presynaptic
459 SNG-1 turnover . These two phenotypes together suggest that there may be homeostatic feedback that
460 adjusts the steady-state abundance based on the turnover rate or vice versa. On the other hand, these
461 genetic manipulations could cause reduced presynaptic abundance of SNG-1 indirectly through
462 regulation of other proteins within the neuron and/or in other cell types within the animal.

463 The steady-state presynaptic SNG-1::ARGO GFP/RFP ratio varies with both neuron identity and
464 age. We interpret this variation primarily as reflecting differences in the proportion of SNG-1::ARGO
465 residing in acidic compartments because (A) sorting into acidic compartments is the canonical route for
466 transmembrane protein degradation, (B) the ratio increases upon injection with Bafilomycin A (Figure 2E)
467 and concanamycin A (Zhong and Richardson, 2025), and (C) the marked difference in presynaptic ratio
468 between VD and DD neurons in L2 larvae is not readily explained with alternate, technical interpretations
469 (Figure 5). Still, we cannot exclude that some factor might contribute to changes in SNG-1::ARGO ratio,
470 such as misfolding of GFP on a subset of newly synthesized SNG-1::ARGO molecules. Importantly, the

471 quantification of SNG-1::ARGO half-life normalizes against the GFP/RFP ratio in age-matched control
472 animals and is therefore unaffected by the variation in steady-state ratio.
473 Positing that the SNG-1::ARGO GFP/RFP ratio mainly reflects sorting into acidic compartments,
474 our data indicate that a large proportion of presynaptic SNG-1 resides in acidic compartments in adult
475 neurons and in newly remodeled DD synapses. These acidic compartments are likely late endosomes
476 and/or autophagosomes. Have these SNG-1 molecules been decommissioned and committed to
477 degradation? This notion seems surprising, yet it aligns with findings from cultured hippocampal neurons
478 showing that SV proteins participate in SV cycling for less than half of their lifetime and, once targeted
479 for degradation, often continue to reside at the presynapse (Truckenbrodt *et al.*, 2018). Moreover, sorting
480 into acidic endosomal compartments need not entail an irreversible exit from the SV cycle: intraluminal
481 vesicles within late endosomes can undergo back-fusion, allowing resident proteins to rejoin the
482 functional pool (Eden and Futter, 2021; Perrin *et al.*, 2021). It is also possible that SNG-1 has an
483 unappreciated function within endosomal compartments. For the DD synapses in L2 larvae in particular,
484 it would be puzzling if SNG-1 were relocated from the original ventral presynapses to the newly
485 generated dorsal presynapses only to be rapidly eliminated.
486 Finally, our data suggest that in at least one *C. elegans* neuron type – the GABAergic motor
487 neuron VD2 – SNG-1 exists in two distinct pools within each presynapse that do not intermix over at
488 least several days. This is surprising because SV cycling is generally thought to intermix vesicle proteins
489 in an endosomal sorting compartment, effectively generating a single pool of SV protein over long
490 timescales. We consider several ways two SNG-1 half-lives could arise. One possibility is that SNG-1
491 resides on two distinct SV pools in the VD2 neuron. To remain chronically distinct, one pool might never
492 participate in neurotransmitter release, the pools might operate in temporally or spatially distinct SV
493 cycling, or one or both pools might exclusively use kiss-and-run fusion, bypassing endosomal sorting.
494 Hints from other experimental animals suggest these scenarios might be plausible. For instance, a
495 synapse can contain a “resting” SV pool that is resistant to recruitment upon strong experimental
496 stimulation, might not cycle under some physiological contexts, and can comprise over half of the SVs in
497 a presynapse (Chanaday *et al.*, 2019). SVs that do release can be further separated into the evoked
498 release versus the spontaneously released pools, and in some contexts, these pools remain segregated
499 for tens of minutes (Sara *et al.*, 2005; Mathew *et al.*, 2008; Andreae *et al.*, 2012; Kavalali, 2014; Egashira
500 *et al.*, 2022). Nonetheless, we are not aware of examples where SV pools retain their distinct identities
501 for days. Another possible explanation is that SNG-1 could itself exist in two distinct forms, such as
502 differential post-translational modification(s) during SNG-1 synthesis or a developmental time-window,
503 with one form resistant to degradation. Various mammalian synaptogyrin isoforms can carry post-
504 translational modifications, though none have been identified for *C. elegans* SNG-1 (iPTMnet)(Huang *et*

505 *al.*, 2018). Further research on this two-phase SNG-1 turnover will illuminate how SV proteins can
506 achieve selective turnover, which could have broad implications for how neurotransmission is tuned.
507
508

509 Materials and Methods

510 *C. elegans* culture and maintenance

511 Nematodes were grown at room temperature on nematode growth media (NGM) plates seeded
512 with *Escherichia coli* OP50. All experiments used hermaphrodite worms and the stages used for each
513 experiment are outlined in each figure legend. Several strains were provided by the Caenorhabditis
514 Genetics Center (CGC), which is funded by NIH Office of Research Infrastructure Program (P40
515 OD010440). The *carIs1(Pglr-4>Flippase)* allele, which flips-on *sng-1::argo* in the DA9 neuron, was
516 generated by integrating *shyEx246* from the Shaul Yogev lab. To induce expression of *heSi160[Pheat-*
517 *shock>Cre]* for the ARGO pulse, worm plates were shifted to a 34 °C incubator for 1 hour. For
518 experiments with *uba-1(it129ts)*, animals were grown at 20 °C, then shifted to 25 °C, the non-permissive
519 temperature, at the L2 larval stage. Consistent with reported phenotypes, these animals at 25 °C were
520 fully sterile. The canonical permissive temperature for *uba-1(it129ts)* is 15 °C, where the allele behaves
521 like a weaker hypomorph; in our hands, the strain is viable and appears grossly wild-type at 20 °C.
522
523 <u>Strains used in this study:</u>
524 PBT68 *bqSi506(Prgef-1>Flp, unc-119(+)) IV; sng-1(syb3140car2) heSi160 X*
525 PBT67 *carIs1(Pglr-4>Flp, Podr-1>rfp) II; sng-1(syb3140car2) heSi160 X*
526 PBT188 *bqSi488(Ptph-1>Flp, unc-119(+) IV; sng-1(syb3140car2) heSi160 X*
527 PBT231 *bqSi542 IV; sng-1(syb3140car2) heSi160 X*
528 PBT84 *sng-1(syb3140car2)*
529 RB503 *sng-1(ok234) X*
530 PBT72 *carIs1 II; sng-1(syb3140car2) X*
531 PBT177 *carIs1 II; uba-1(it129) IV; sng-1(syb3140car2) heSi160 X*
532 PBT58 *bqSi542(Punc-47>Flp, unc-119(+) IV; sng-1(syb3140) heSi160 X*
533

534 Genome editing using CRISPR/Cas9

535 The initial ARGO allele, *sng-1(syb3140)*, consisting of *FRT-stop+3'utr-FRT-RFP-loxP-GFP-loxP,*
536 was generated by SunyBiotech. We determined that the resulting SNG-1::RFP::GFP was destabilized
537 and had accelerated degradation. Removal of GFP upon ARGO activation led to increased RFP

538 fluorescence intensity up to the expected intensity based on existing strains (Schwartz and Jorgensen,
539 2016), indicating that the amino acid linker between the RFP and GFP was causing the destabilization.
540 We therefore used CRISPR/Cas9 to modify the amino acid linker between the RFP and GFP in the *sng-*
541 *1(syb3140)* allele, generating the *sng-1(syb3140car2)* allele, which fixed the destabilization. The
542 *syb3140car2* allele was used in all experiments in this study with two exceptions: Fig S1M, which
543 quantifies the rate of Cre-mediated recombination, and Table 1, which quantifies Cre/loxP specificity and
544 efficacy. Both of these parameters are expected to be identical between *syb3140* and *syb3140car2*. The
545 *car2* allele was generated following the protocol in (Paix *et al.*, 2015). A ssDNA with 36 and 38 bp
546 homology on either side was used for the repair template (Ultramer, Integrated DNA Technologies
547 (IDT)). Two cRNAs (IDT) were used, one on either end of the edit. The genomic sequence of the *argo*
548 cassette and the cDNA sequences of *sng-1::argo* before and after the removal of *GFP* are provided
549 Figures S4-6.
550

551 **Aldicarb assay**

552 Aldicarb assays were performed as described (Mahoney et al., 2006). Briefly, 30 Day 1 adults of
553 each strain were placed on a plate containing 0.5 mM aldicarb, and they were periodically assessed for
554 paralysis visually after touch with an eyelash. Plates were scored blind to genotype, and the experiment
555 was executed in three biological replicates, each on a separate day.
556

557 **qPCR of genomic DNA**

558 Day 0/L4 animals of the genotype *bqSi542; sng-1(syb3140) heSi160* were shifted to 34 °C for 1
559 hour at Time = 0. Directly before the shift, and at the indicated times afterward, approximately 50
560 animals were picked and lysed with the standard worm lysis protocol. Relative abundance of the Cre-
561 recombined locus was assess using primers that aligned to the 3' end of *RFP* before the first *loxP* and
562 the 3' end of *sng-1* after the second *loxP.* Relative transcript abundance was calculated using the ΔΔCt
563 method, with primers against *gpi-1* used as the internal control. All reactions were performed in triplicate.
564

565 **RNA extraction and qPCR**

566 Total RNA was extracted from *Caenorhabditis elegans* samples using the TRI reagent (Sigma
567 Aldrich), ethanol precipitation protocol. The LunaScript Kit (NEB) was used for complementary DNA
568 (cDNA) synthesis according to the manufacturer's protocol. Quantitative RT-PCR was performed using
569 the Roche Lightcycler 480. Primers for the target genes (*sng-1, hsp-16*) and the reference/normalization
570 gene (*pmp-42*) were validated empirically for specificity and efficiency. Melting curve analysis was
571 performed at the end of each run to confirm amplification specificity. Gene expression levels were

572 calculated using the ΔΔCt method, with the *pmp-42* gene serving as the internal control. All reactions
573 were performed in triplicate.
574
575 **Bafilomycin A treatment**
576 Bafilomycin A was injected into the body cavity of *C. elegans* similarly to previous work
577 (Wilkinson et al., 2015). Briefly, 25 μM of BafA in 5% DMSO or 0.2% DMSO ("mock") was co-injected
578 with Orange G for color into the pseudocoelom, and animals were allowed to recover for three hours
579 before they were imaged with fluorescence confocal microscopy as described above. BafA injected
580 animals were still moving when they were put on slides, indicating that the BafA had not completely
581 blocked V-ATPase function.
582
583 **Assessing specificity and efficacy of the pulse**
584 To assess the efficacy and specificity of Heat-shock>Cre-mediated recombination of *GFP* from
585 the ARGO cassette (Table 1), fluorescence was scored based on visualizing SNG-1::ARGO GFP and
586 RFP fluorescence at least 3 days after activation. Scoring was performed using a combination of two
587 approaches: 1) qualitative assessment by eye on a compound fluorescent microscope, wherein the
588 experimenter performed an initial visual assessment of a subset of animals and then binned all of the
589 animals in the cohort as either "bright" (no recombination) or "dim" (recombination); 2) semi-quantitative
590 assessment on the spinning disk confocal microscope, wherein the animals were imaged with
591 standardized microscope settings, raw fluorescence intensity and GFP/RFP values were assessed for a
592 subset of animals, and then all animals in the cohort were binned as "ratio high" (no recombination) or
593 "ratio low"(recombination). The distribution of GFP/RFP ratios in all instances was bimodal; if an animal
594 appeared to have an intermediate value, which occurred in about 1-5% of individuals, that animal was
595 not scored.
596
597 **Microscopy and imaging**
598 Worms were mounted on 3% freshly made agarose pads into drops of 20 mM levamisole. An
599 imaging system comprised of a Nikon Eclipse Ti2 microscope, Yokogawa CSU-W1 SoRa spinning-disk
600 unit and a Hamamatsu ORCA-fusionBT digital camera C15440 with Plan Apo x60 A1/2 Nikon objective
601 with water immersion was used to acquire all images. Image settings (60% of laser power and 200 ms
602 exposure time) were identical for all groups and treatments across experiments. Z-stacks were taken
603 with 0.4 μm step in the 20-30 μm range, depending on type of neuron. For super resolution by optical
604 reassignment (Figure 1I), the 2.8x SoRa magnifier was used, z-stacks were acquired with 0.3 μm steps,
605 and images were deconvoluted in post-processing.

606

607 **Microscopy data analysis**

608 Nd2 files were screened with NIS Elements Software for unusually low signal, severe movement
609 or drifting and discarded, the rest images were processed with Fiji (ImageJ) software. Image stacks were
610 transformed using z-projection function with max intensity option, areas of interest were selected either
611 with Rectangle tool (for cell bodies) or Segmented line and Straighten function (for synaptic areas). For
612 each image, a Threshold was applied with default settings to the RFP channel, and the Analyze Particles
613 function was used to identify ROIs in that thresholded image. These ROIs were then used to quantify
614 fluorescence from both the RFP and GFP channels. The mean intensity of each channel was used for all
615 calculations. Each obtained array of values in csv format was united in a single data frame, and synaptic
616 puncta less than 0.1 μm^2 (for the wild-type DA9 and NSM datasets) or 0.2 μm^2 (for the VD, DD, and
617 *uba-1* mutant datasets) were filtered out due to high variability in relative RFP:GFP fluorescence
618 intensities. This high variability was likely due to low signal-to-noise; a major contributing factor to the
619 noise was autofluorescence. The GFP/RFP ratio calculation was done for each presynapse with Jupyter
620 Notebook and Python scripts.

621 To find the average presynaptic GFP/RFP ratio per neuron, all the individual GFP/RFP ratios
622 within the presynaptic region of a neuron were averaged.

623 To find the average presynaptic GFP/RFP ratio by position along the proximal-distal axis, the
624 length of each neuron's presynaptic region was divided into the most proximal 30%, the most distal 30%
625 and the middle 40%, and all the presynaptic puncta within each domain was averaged.

626

627 **Statistical Analyses**

628 Prism GraphPad software was used to generate all plots and perform most statistical analyses.
629 The rest of the statistical analyses were performed in Rstudio as noted below.

630

631 **Assessing the effective timing of the pulse from microscopy data**

632 To test whether the SNG-1::ARGO GFP/RFP decreased significantly by 4 hours after the heat-
633 shock (Figure S1F-L), we used a linear mixed-effects model with treatment (no heat-shock vs 4 hours
634 post heat-shock) as a fixed effect and worm as a random effect to include the GFP/RFP ratio
635 measurements for each presynapse and account for multiple measurements per animal (lmer function,
636 lme4 package). Residual diagnostics were assessed using the DHARMa package. For DA9 D2 and D6
637 (Figure S1H, J), data were log transformed to meet model assumptions, and the back-transformed mean
638 GFP/RFP per animal are plotted. For DA9 D2 with *heSi160* (Figure S1H), residual plots with the log
639 transform still showed a deviation from normality (KS test: ns, Dispersion test: ns, outlier test, $p = 0.012$),

but model assumptions were considered adequately met given the large sample size and consistency of results across multiple statistical approaches, including nonparametric tests. For NSM D2 (Figure S1K), data were square-root transformed to meet model assumptions, and the back-transformed mean GFP/RFP per animal are plotted. Empirically, this transformation was the closest to fitting model assumptions, though residual plots still showed some deviation from normality (KS test: ns, Dispersion test: ns, outlier test, p = 0.016). For VD2 D2 (Figure S1L), data did not fit the assumptions of the linear mixed model and an adequate transformation could not be found, so the mean SNG-1 ARGO GFP/RFP ratio per animal was analyzed using a two-sided t test (the data distribution was not significantly different from a normal distribution).

As another approach to assess whether and to what extent a cell sometimes ectopically recombines one of the two alleles of *sng-1::argo*, we compared the average presynaptic SNG-1::ARGO GFP/RFP mean and standard deviation in the DA9 neuron between a strain with vs without *heSi160[Pheat-shock>Cre]* and saw no significant difference (Figure S1A).

As a third approach to assess specificity and efficacy of recombination, we compared the interneuronal coefficient of variation (CV) in the presynaptic SNG-1::ARGO GFP/RFP between control versus pulsed groups. We calculated the CV for control versus heat-shocked groups at each timepoint for each neuron class. As there is one CV value per neuron class, treatment, and timepoint, these comparisons are qualitative. If the CV is roughly constant in the non-pulsed group over time, it would suggest that there is not much ectopic recombination without the pulse treatment. Similarly, if the CV is roughly constant in the pulsed group over time, it would suggest that recombination is uniformly completed in both alleles of each animal. *I haven't added this yet. It would be most useful to include the version with all data vs after outliers are removed. Is this necessary?*

Assessing Variance

To assess variability in SNG-1::ARGO GFP/RFP ratios across synapses within individual neurons (intraneuronal variance), because the data roughly followed a lognormal distribution, we used Rstudio to calculate the CV as:

$$CVlog = \sqrt{\{e^{\sigma^2} - 1\}}$$

Then, average of all CVs per worm was compared between days using Kruskal-Wallis test, because the data were nonparametric, with Dunn's multiple comparisons test.

673 **Fitting decay curves to turnover data**

674 Each SNG-1::ARGO GFP/RFP datapoint from the turnover experiments is the mean of all the
675 GFP/RFP ratios from each presynaptic puncta detected in a single animal. Those datapoints were
676 normalized by the mean presynaptic GFP/RFP ratio from an age-matched control (non-pulsed) cohort of
677 animals that was imaged in parallel. In this way, the steady-state changes in presynaptic SNG-1::ARGO
678 GFP/RFP ratio by animal age do not impact the turnover calculations. SNG-1::ARGO half-life was
679 calculated using Prism to fit a one-phase exponential decay curve to the data. The curves were fitted
680 using least squares regression with no weighting, considering each replicate Y value as an individual
681 point. Outliers were detected and eliminated with Q = 5% (DA9), 1% (NSM), 0r 3% (VD2). These values
682 were selected based on the data in Table 1, which assessed the frequency of ectopic *gfp* excision in the
683 absence of the heat-shock pulse, and the frequency of failed *GFP* excision following the heat-shock
684 pulse, for each neuron identity. Unless otherwise noted, we constrained the plateau to the experimentally
685 determined value based on background GFP fluorescence, which comes from autofluorescence. This
686 was measured from the adult Day 7 images for each of the three neuron identities by hand-selecting the
687 synaptic region in the RFP channel, copying it to the GFP channel, shifting the selection to a position
688 adjacent to the synapses, then finding the GFP fluorescence intensities inside the ROIs. Goodness of fit
689 was quantified with R squared.

690

691 **Assessing VD2 turnover**

692 We noticed that for the VD2 neuron, the presynaptic SNG-1::ARGO GFP/RFP ratio does not
693 appear to approach the background in the turnover experiment. Indeed, a two-phase exponential decay
694 function improves the curve fit, from an R squared of 0.41 to 0.48, and comparing the one-phase versus
695 two-phase functions using extra sum-of-squares F test showed that the two-phase curve was
696 significantly favored (Null hypothesis: one phase decay, alternative hypothesis: two phase decay, P =
697 0.0175). A two-phase exponential decay function will often produce a better fit than a one-phase function
698 due to its additional parameters. Therefore, we took a second approach to assess whether the one-
699 phase decay function could be ruled out using the same dataset: we compared the predicted plateau
700 value from the one-phase function versus the measured background. Specifically, we fit a one-phase
701 exponential decay function to the data without constraining the plateau. We compared the best-fit
702 plateau and 95% C.I. from that function to the mean background and 95% C.I. calculated from the
703 microscopy images (as described above)(Figure 4B). Indeed, the one-phase curve plateaus above the
704 background, and the 95% C.I.s do not overlap (Figure 4B). Furthermore, in Figure 4D, we use the best-fit
705 parameters from the two-phase exponential decay function from the VD2 turnover dataset in Figure 4A
706 to predict the presynaptic GFP/RFP ratio 5 days after the pulse (the Model 1, D2 bar). That predicted

707 value matched the real value ± SEM from a separate experiment, showing that this result is robust (the
708 Results A2 bar).
709 Given that we could not find evidence for different turnover rates between individual presynaptic
710 puncta within the VD2 neuron (Figure 4C), we considered two explanations for the two-phase turnover
711 kinetics of SNG-1::ARGO within individual VD2 presynapses:
712 Model 1: there are two chronically distinct pools of SNG-1 protein
713 Model 2: there is a time-dependent suppression of turnover
714 We generated predictions from the two proposed models as described below. Then, we compared those
715 predictions qualitatively to an experiment in which we pulsed the VD2 SNG-1::ARGO at adult D2 versus
716 D4 of adulthood and imaged at D7 (Figure 4D). In order to prevent datapoints from inefficient or
717 spontaneous Cre-mediated recombination from skewing the results, we censored aberrant data points
718 as follows: the median presynaptic GFP/RFP ratio was calculated for each set of A7 animals imaged
719 (one data point per animal, which was the mean GFP/RFP ratio across all VD2 presynaptic puncta for
720 that animal): control, pulse at A2, pulse at A4 (all incubated at 20 °C), and control versus pulse at A2 and
721 incubated at 25 °C. For the A7 controls, datapoints lower than the median ratio for the pulse at A4 group
722 were censored (3 of 51 for the 20 °C controls, 0 of 20 for the 25 °C controls). For all three pulsed groups,
723 datapoints higher than the median ratio for the control A7 group at the corresponding temperature were
724 censored (6 of 44, 13.6% for A2 pulse; 6 of 19 for the A4 pulse; 3 of 29 for the A2 pulse and 25 °C
725 incubation).
726
727 **I. Assessing Model I: that there are two distinct populations of SNG-1 with different turnover**
728 **kinetics at each synapse**
729 Using the best-fit values from the two-phase exponential decay function from the data in Figure
730 4D, we predicted the presynaptic GFP/RFP ratio 3 days and 5 days after the pulse using ChatGTP 5.
731
732 **II. Assessing Model 2: that turnover is suppressed during the course of the turnover**
733 **experiment**
734 In this model, all presynaptic SNG-1::ARGO is initially subject to fast-phase turnover, but this
735 turnover becomes inhibited or dysfunctional at a specific time in the animal's life, which occurs during the
736 course of the turnover experiment when the pulse is at A2. In this model, only protein that undergoes
737 fast-phase turnover prior to the onset of inhibition is degraded; all remaining protein is retained with
738 unappreciable turnover thereafter. In other words, the final GFP/RFP ratio reflects the amount of SNG-
739 1::ARGO that experienced degradation before the inhibition/dysfunction event. For the fast-phase, k =

740 0.7535 day^{-1}. Solving for the time at which 60% of the protein remains gives 0.66 d after the pulse, which
741 would equate to A2.66.
742
743

744 Data availability

745 Strains and plasmids are available upon request. Microscopy images will be deposited in BioImage
746 Archive.
747
748
749

750 Acknowledgments

751 Some strains were provided by the *Caenorhabditis* elegans Genetics Center (CGC), which is funded by
752 the National Institutes of Health (NIH) Office of Research Infrastructure Programs (P40 OD010440). The
753 Shaul Yogev lab provided *shyEx246*, which was integrated to generate *carIs1*. We thank Michael O.
754 Harding from the Statistical Consulting group at the University of Wisconsin – Madison for assistance in
755 data analysis. We thank Julianna Miller, Emma Keep, Adam Darlington, Margaret Brener, and Sophia
756 Whitley for assistance in the lab. We thank Ruben H. Land and David M. Lipton for feedback on the
757 manuscript. This work was supported by the National Institutes of Health (NIH) grant R35 GM154869 to
758 C.E.R.
759
760
761

762 References

763 Abraham, C, Bai, L, and Leube, RE (2011). Synaptogyrin-dependent modulation of synaptic
764 neurotransmission in *Caenorhabditis elegans*. Neuroscience 190, 75–88.
765
766 Andreae, LC, Fredj, N Ben, and Burrone, J (2012). Independent vesicle pools underlie different modes of
767 release during neuronal development. Journal of Neuroscience 32, 1867–1874.
768
769 Binotti, B, Pavlos, NJ, Riedel, D, Wenzel, D, Vorbrüggen, G, Schalk, AM, Kühnel, K, Boyken, J, Erck, C,
770 Martens, H, et al. (2014). The GTPase RaB26 links synaptic vesicles to the autophagy pathway. Elife
771 2015, 1–23.
772

773 Birdsall, V, Kirwan, K, Zhu, M, Imoto, Y, Wilson, SM, Watanabe, S, and Waites, CL (2022). Axonal
774 transport of Hrs is activity dependent and facilitates synaptic vesicle protein degradation. Life Science
775 Alliance 5.
776
777 Bojkowska, K, Santoni De Sio, F, Barde, I, Offner, S, Verp, S, Heinis, C, Johnsson, K, and Trono, D
778 (2011). Measuring *in vivo* protein half-life. Chem Biol 18, 805–815.
779
780 Bulovaite, E, Qiu, Z, Kratschke, M, Zgraj, A, Fricker, DG, Tuck, EJ, Gokhale, R, Koniaris, B, Jami, SA,
781 Merino-Serrais, P, et al. (2022). A brain atlas of synapse protein lifetime across the mouse lifespan.
782 Neuron 110, 4057-4073.e8.
783
784 Ceccarelli, B, Hurlbut, WP, and Mauro, A (1973). Turnover of transmitter and synaptic vesicles at the
785 frog neuromuscular junction. Journal of Cell Biology 57, 499–524.
786
787 Chanaday, NL, Cousin, MA, Milosevic, I, Watanabe, S, and Morgan, JR (2019). The synaptic vesicle
788 cycle revisited: new insights into the modes and mechanisms. J Neurosci 39, 8209–8216.
789
790 Cohen, LD, Zuchman, R, Sorokina, O, Müller, A, Dieterich, DC, Armstrong, JD, Ziv, T, and Ziv, NE
791 (2013). Metabolic turnover of synaptic proteins: kinetics, interdependencies and implications for synaptic
792 maintenance. PLoS One 8, e63191.
793
794 Depuydt, G, Shanmugam, N, Rasulova, M, Dhondt, I, and Braeckman, BP (2016). Increased protein
795 stability and decreased protein turnover in the *Caenorhabditis elegans* Ins/IGF-1 *daf-2* mutant. J
796 Gerontol A Biol Sci Med Sci 71, 1553.
797
798 Dörrbaum, AR, Kochen, L, Langer, JD, and Schuman, EM (2018). Local and global influences on protein
799 turnover in neurons and glia. Elife 7.
800
801 Eden, ER, and Futter, CE (2021). Membrane trafficking: Retrofusion as an escape route out of the
802 endosome. Current Biology 31, R1037–R1040.
803
804 Egashira, Y, Kumade, A, Ojida, A, and Ono, F (2022). Spontaneously recycling synaptic vesicles
805 constitute readily releasable vesicles in intact neuromuscular synapses. Journal of Neuroscience 42,
806 3523–3536.

807
808 Fernandes, AC, Uytterhoeven, V, Kuenen, S, Wang, YC, Slabbaert, JR, Swerts, J, Kasprowicz, J, Aerts,
809 S, and Verstreken, P (2014). Reduced synaptic vesicle protein degradation at lysosomes curbs
810 TBC1D24/sky-induced neurodegeneration. Journal of Cell Biology 207, 453–462.
811
812 Foot, N, Henshall, T, and Kumar, S (2017). Ubiquitination and the regulation of membrane proteins.
813 Physiol Rev 97, 253–281.
814
815 Fornasiero, EF, Mandad, S, Wildhagen, H, Alevra, M, Rammner, B, Keihani, S, Opazo, F, Urban, I,
816 Ischebeck, T, Sakib, MS, et al. (2018). Precisely measured protein lifetimes in the mouse brain reveal
817 differences across tissues and subcellular fractions. Nature Communications 2018 9:1 9, 1–17.
818
819 Gems, D, and Riddle, DL (2000). Defining wild-type life span in *Caenorhabditis elegans*. The Journals of
820 Gerontology: Series A 55, B215–B219.
821
822 Grill, B, Bienvenut, W V., Brown, HM, Ackley, BD, Quadroni, M, and Jin, Y (2007). *C. elegans* RPM-1
823 regulates axon termination and synaptogenesis through the Rab GEF GLO-4 and the Rab GTPase
824 GLO-1. Neuron 55, 587–601.
825
826 Hallam, SJ, and Jin, Y (1998). *lin-14* regulates the timing of synaptic remodelling in *Caenorhabditis*
827 *elegans*. Nature 395, 78–82.
828
829 Heo, S, Diering, GH, Na, CH, Nirujogi, RS, Bachman, JL, Pandey, A, and Huganir, RL (2018).
830 Identification of long-lived synaptic proteins by proteomic analysis of synaptosome protein turnover. Proc
831 Natl Acad Sci U S A 115, E3827–E3836.
832
833 Herzog, E, Nadrigny, F, Silm, K, Biesemann, C, Helling, I, Bersot, T, Steffens, H, Schwartzmann, R,
834 Valentin Nägerl, U, El Mestikawy, S, et al. (2011). In vivo imaging of intersynaptic vesicle exchange
835 using VGLUT1Venus knock-in mice. Journal of Neuroscience 31, 15544–15559.
836
837 Hipp, MS, Kasturi, P, and Hartl, FU (2019). The proteostasis network and its decline in ageing. Nature
838 Reviews Molecular Cell Biology 2019 20:7 20, 421–435.
839

840 Hoffmann-Conaway, S, Brockmann, MM, Schneider, K, Annamneedi, A, Rahman, KA, Bruns, C,
841 Textoris-Taube, K, Trimbuch, T, Smalla, KH, Rosenmund, C, et al. (2020). Parkin contributes to synaptic
842 vesicle autophagy in bassoon-deficient mice. Elife 9, 1–30.
843
844 Huang, H, Arighi, CN, Ross, KE, Ren, J, Li, G, Chen, SC, Wang, Q, Cowart, J, Vijay-Shanker, K, and
845 Wu, CH (2018). IPTMnet: An integrated resource for protein post-translational modification network
846 discovery. Nucleic Acids Res 46, D542–D550.
847
848 Jin, EJ, Kiral, FR, Ozel, MN, Burchardt, LS, Osterland, M, Epstein, D, Wolfenberg, H, Prohaska, S, and
849 Hiesinger, PR (2018). Live observation of two parallel membrane degradation pathways at axon
850 terminals. Curr Biol 28, 1027-1038.e4.
851
852 Kavalali, ET (2014). The mechanisms and functions of spontaneous neurotransmitter release. Nature
853 Reviews Neuroscience 2014 16:1 16, 5–16.
854
855 Klassen, MP, Wu, YE, Maeder, CI, Nakae, I, Cueva, JG, Lehrman, EK, Tada, M, Gengyo-Ando, K,
856 Wang, GJ, Goodman, M, et al. (2010). An Arf-like small G protein, ARL-8, promotes the axonal transport
857 of presynaptic cargoes by suppressing vesicle aggregation. Neuron 66, 710–723.
858
859 Kluever, V, Russo, B, Mandad, S, Kumar, NH, Alevra, M, Ori, A, Rizzoli, SO, Urlaub, H, Schneider, A,
860 and Fornasiero, EF (2022). Protein lifetimes in aged brains reveal a proteostatic adaptation linking
861 physiological aging to neurodegeneration. Sci Adv 8, 4437.
862
863 Kulkarni, M, and Smith, HE (2008). E1 ubiquitin-activating enzyme UBA-1 plays multiple roles throughout
864 *C. elegans* Development. PLoS Genet 4, e1000131.
865
866 Kurup, N, Yan, D, Goncharov, A, and Jin, Y (2015). Dynamic microtubules drive circuit rewiring in the
867 absence of neurite remodeling. Current Biology 25, 1594–1605.
868
869 LaVail, MM, and LaVail, JH (1975). Retrograde intra-axonal transport of horseradish peroxidase in retinal
870 ganglion cells of the chick. Brain Res 85, 273–280.
871
872 Lipton, DM, Maeder, CI, and Shen, K (2018). Rapid assembly of presynaptic materials behind the growth
873 cone in dopaminergic neurons is mediated by precise regulation of axonal transport. Cell Rep 24, 2709.

874
875 Liu, Y, Beyer, A, and Aebersold, R (2016). On the dependency of cellular protein levels on mRNA
876 abundance. Cell 165, 535–550.
877
878 López-Otín, C, Blasco, MA, Partridge, L, Serrano, M, and Kroemer, G (2023). Hallmarks of aging: An
879 expanding universe. Cell 186, 243–278.
880
881 Maeder, CI, San-Miguel, A, Wu, EY, Lu, H, and Shen, K (2014). In vivo neuron-wide analysis of synaptic
882 vesicle precursor trafficking. Traffic 15, 273–291.
883
884 Mahoney, TR, Luo, S, and Nonet, ML (2006). Analysis of synaptic transmission in *Caenorhabditis*
885 *elegans* using an aldicarb-sensitivity assay. Nature Protocols 2006 1:4 1, 1772–1777.
886
887 Mathew, SS, Pozzo-Miller, L, and Hablitz, JJ (2008). Kainate modulates presynaptic GABA release from
888 two vesicle pools. Journal of Neuroscience 28, 725–731.
889
890 Mathieson, T, Franken, H, Kosinski, J, Kurzawa, N, Zinn, N, Sweetman, G, Poeckel, D, Ratnu, VS,
891 Schramm, M, Becher, I, et al. (2018). Systematic analysis of protein turnover in primary cells. Nature
892 Communications 2018 9:1 9, 1–10.
893
894 Muñoz-Jiménez, C, Ayuso, C, Dobrzynska, A, Torres-Mendéz, A, Ruiz, PDLC, and Askjaer, P (2017). An
895 efficient flp-based toolkit for spatiotemporal control of gene expression in *Caenorhabditis elegans*.
896 Genetics 206, 1763–1778.
897
898 Neisch, AL, Neufeld, TP, and Hays, TS (2017). A STR IPAK complex mediates axonal transport of
899 autophagosomes and dense core vesicles through PP2A regulation. Journal of Cell Biology 216, 441–
900 461.
901
902 Okerlund, ND, Schneider, K, Leal-Ortiz, S, Montenegro-Venegas, C, Kim, SA, Garner, LC, Gundelfinger,
903 ED, Reimer, RJ, and Garner, CC (2017). Bassoon controls presynaptic autophagy through Atg5. Neuron
904 93, 897-913.e7.
905

906 Paix, A, Folkmann, A, Rasoloson, D, and Seydoux, G (2015). High efficiency, homology-directed
907 genome editing in *Caenorhabditis elegans* using CRISPR-Cas9 ribonucleoprotein complexes. Genetics
908 201, 47–54.
909
910 Park, M, Watanabe, S, Poon, VYN, Ou, CY, Jorgensen, EM, and Shen, K (2011). CYY-1/Cyclin Y and
911 CDK-5 differentially regulate synapse elimination and formation for rewiring neural circuits. Neuron 70,
912 742.
913
914 Perrin, P, Janssen, L, Janssen, H, van den Broek, B, Voortman, LM, van Elsland, D, Berlin, I, and
915 Neefjes, J (2021). Retrofusion of intralumenal MVB membranes parallels viral infection and coexists with
916 exosome release. Current Biology 31, 3884.
917
918 Price, JC, Guan, S, Burlingame, A, Prusiner, SB, and Ghaemmaghami, S (2010). Analysis of proteome
919 dynamics in the mouse brain. Proc Natl Acad Sci U S A 107, 14508–14513.
920
921 Raja, MK, Preobraschenski, J, Olmo-Cabrera, S Del, Martinez-Turrillas, R, Jahn, R, Perez-Otano, I, and
922 Wesseling, JF (2019). Elevated synaptic vesicle release probability in synaptophysin/gyrin family
923 quadruple knockouts. Elife 8.
924
925 Reddien, PW (2024). The purpose and ubiquity of turnover. Cell 187, 2657–2681.
926
927 Rodriguez, EA, Campbell, RE, Lin, JY, Lin, MZ, Miyawaki, A, Palmer, AE, Shu, X, Zhang, J, and Tsien,
928 RY (2017). The growing and glowing toolbox of fluorescent and photoactive proteins. Trends Biochem
929 Sci 42, 111–129.
930
931 Sara, Y, Virmani, T, Deák, F, Liu, X, and Kavalali, ET (2005). An isolated pool of vesicles recycles at rest
932 and drives spontaneous neurotransmission. Neuron 45, 563–573.
933
934 Schwartz, ML, and Jorgensen, EM (2016). SapTrap, a toolkit for high-throughput CRISPR/Cas9 gene
935 modification in *Caenorhabditis elegans.* Genetics 202, 1277–1288.
936
937 Sheehan, P, and Waites, CL (2019). Coordination of synaptic vesicle trafficking and turnover by the
938 Rab35 signaling network. Small GTPases 10, 54–63.
939

940 Sheehan, P, Zhu, M, Beskow, A, Vollmer, C, and Waites, CL (2016). Activity-dependent degradation of
941 synaptic vesicle proteins requires Rab35 and the ESCRT pathway. Journal of Neuroscience 36, 8668–
942 8686.
943
944 Soukup, SF, Kuenen, S, Vanhauwaert, R, Manetsberger, J, Hernández-Díaz, S, Swerts, J, Schoovaerts,
945 N, Vilain, S, Gounko, N V., Vints, K, et al. (2016). A LRRK2-dependent endophilinA phosphoswitch is
946 critical for macroautophagy at presynaptic terminals. Neuron 92, 829–844.
947
948 Staras, K, Branco, T, Burden, JJ, Pozo, K, Darcy, K, Marra, V, Ratnayaka, A, and Goda, Y (2010). A
949 vesicle super-pool spans multiple presynaptic terminals in hippocampal neurons. Neuron 66, 37–44.
950
951 Stavoe, AKH, Hill, SE, Hall, DH, and Colón-Ramos, DA (2016). KIF1A/UNC-104 transports ATG-9 to
952 regulate neurodevelopment and autophagy at synapses. Dev Cell 38, 171–185.
953
954 Toyama, BH, Savas, JN, Park, SK, Harris, MS, Ingolia, NT, Yates, JR, and Hetzer, MW (2013).
955 Identification of long-lived proteins reveals exceptional stability of essential cellular structures. Cell 154.
956
957 Truckenbrodt, S, Viplav, A, Jähne, S, Vogts, A, Denker, A, Wildhagen, H, Fornasiero, EF, and Rizzoli,
958 SO (2018). Newly produced synaptic vesicle proteins are preferentially used in synaptic transmission.
959 EMBO J 37.
960
961 Uytterhoeven, V, Kuenen, S, Kasprowicz, J, Miskiewicz, K, and Verstreken, P (2011). Loss of Skywalker
962 reveals synaptic endosomes as sorting stations for synaptic vesicle proteins. Cell 145, 117–132.
963
964 Visscher, M, De Henau, S, Wildschut, MHE, van Es, RM, Dhondt, I, Michels, H, Kemmeren, P, Nollen,
965 EA, Braeckman, BP, Burgering, BMT, et al. (2016). Proteome-wide changes in protein turnover rates in
966 *C. elegans* models of longevity and age-related disease. Cell Rep 16, 3041–3051.
967
968 White, JG, Albertson, DG, and Anness, MAR (1978). Connectivity changes in a class of motoneurone
969 during the development of a nematode. Nature 271, 764–766.
970
971 White, JG, Southgate, E, Thomson, JN, and Brenner, S (1986). The structure of the nervous system of
972 the nematode *Caenorhabditis elegans*. Philos Trans R Soc Lond B Biol Sci 314, 1–340.
973

974 Winckler, B, Faundez, V, Maday, S, Cai, Q, Guimas Almeida, C, and Zhang, H (2018). The
975 endolysosomal system and proteostasis: from development to degeneration. J Neurosci 38, 9364–9374.
976
977 Wu, YE, Huo, L, Maeder, CI, Feng, W, and Shen, K (2013). The balance between capture and
978 dissociation of presynaptic proteins controls the spatial distribution of synapses. Neuron 78, 994–1011.
979
980 Yin, Z, Popelka, H, Lei, Y, Yang, Y, and Klionsky, DJ (2020). The roles of ubiquitin in mediating
981 autophagy. Cells 9, 2025.
982
983 Zhang, L, Gurskaya, NG, Merzlyak, EM, Staroverov, DB, Mudrik, NN, Samarkina, ON, Vinokurov, LM,
984 Lukyanov, S, and Lukyanov, KA (2007). Method for real-time monitoring of protein degradation at the
985 single cell level. Biotechniques 42, 446–450.
986
987 Zhong, R, and Richardson, CE (2025). Expansion of lysosomal capacity in early adult neurons driven by
988 TFEB/HLH-30 protects dendrite maintenance during aging in *Caenorhabditis elegans*. PLoS Biol 23,
989 e3002957.
990
991 Zhou, P (2004). Determining protein half-lives. Methods Mol Biol 284, 67–77.

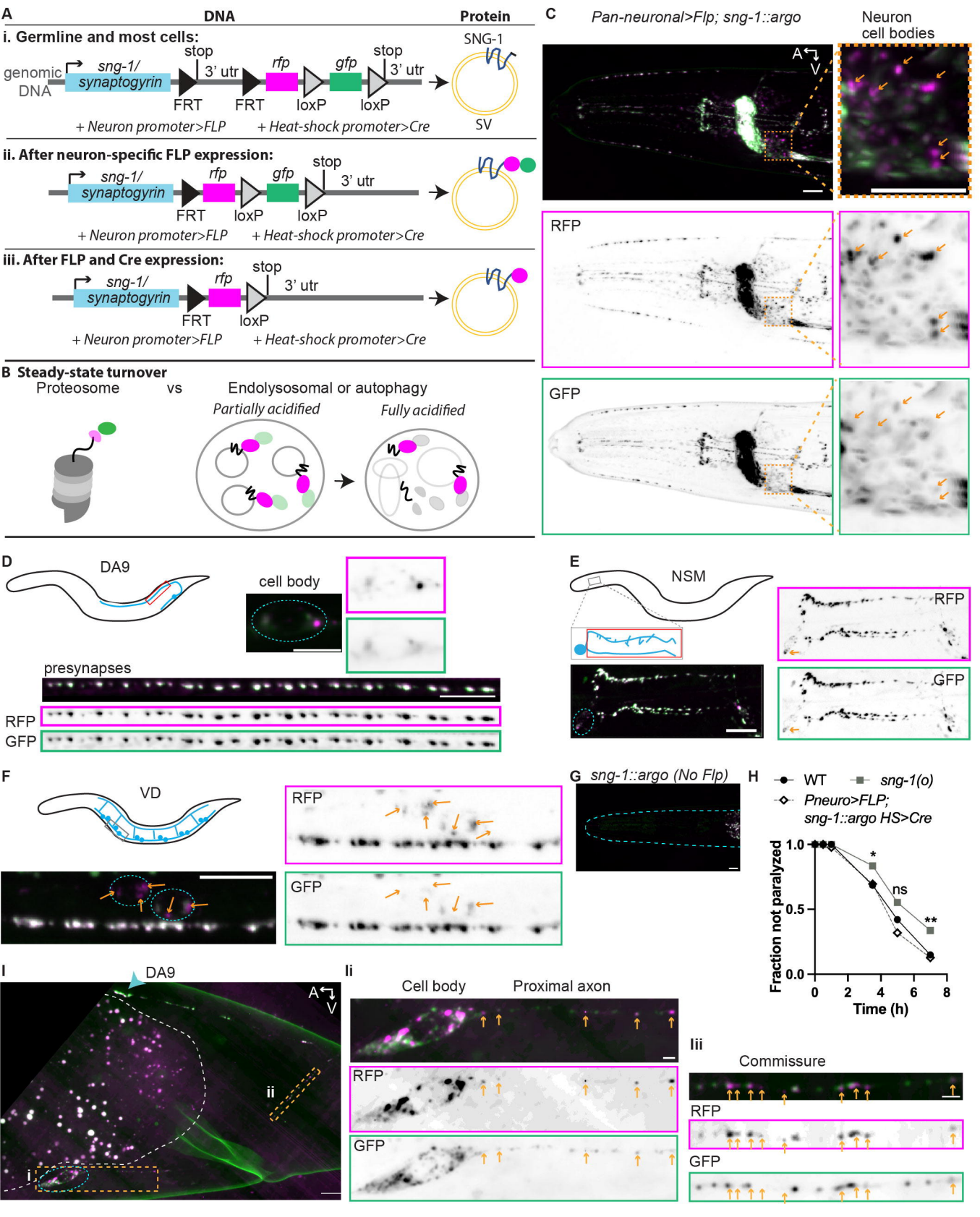

Figure 1. Steady-state SNG-1::ARGO fluorescence indicates that SNG-1 is degraded in lysosomal compartments in the cell body. (A-B) ARGO method overview. (Ai) The argo gene cassette is inserted into the gene-of-interest, ideally at the endogenous genomic locus. The strain also contains transgenes encoding neuron-specific FLP (Flippase) and a mechanism for inducible Cre expression. In this case, we tagged sng-1 at the genomic locus using CRISPR/Cas9 and used a heat-shock promoter to induce Cre expression. (right) The protein-of-interest, in this case SNG-1, will be expressed with a short additional amino acid tag, which is encoded by the first FRT (Figure 1 continued) sequence, in every cell. (Aii) Neuron-specific promoter drives Flp expression shortly after neuron birth. These cells "turn on" the ARGO tag. (Aiii) (left) A pulse of Cre expression removes gfp from the argo gene cassette. This "activates" the ARGO. (right) All newly synthesized SNG-1 will be tagged with RFP. Therefore, RFP fluorescence reports total SNG-1 protein, whereas GFP reports "old" SNG-1. (B) Steady-state imaging provides clues as to how, and sometimes where, a protein-of-interest is degraded. For ARGO-tagged proteins that are degraded in lysosomal compartments, protein that have been sorted for degradation will show stronger RFP vs GFP fluorescence, as GFP is quenched by the acidic environment of the endolysosomal and/or autolysosomal lumen. (C) Representative image of the head of an animal with the sng-1::argo allele in which the ARGO tag is flipped-on by a pan-neuronally expressed FLP, showing co-localized RFP and GFP fluorescence at presynapses throughout the nervous system. Zoomed-in views on the right shows a region where neuron cell bodies reside. Arrows point to endosomes with relatively brighter RFP vs GFP intensity. Scale = 10 ⊠m (D-F) SNG-1::ARGO Flipped-on in individual neurons. Cartoons show neuron morphology (blue) within the animal (black). Red box shows where presynapses are located (D-E), gray boxes indicate the region imaged (E-F), and teal dashed ovals encircle neuron cell bodies (D-F). The VD neurons (F) make a string of en passant synapses along the ventral nerve cord. (G) In the absence of FLP expression, there is no detectable SNG-1::ARGO fluorescence. Teal dashed curve outlines the nose of the animal. (H) Sensitivity to 0.5 mM aldicarb in Day 1 adults (A1) (*P<0.05, **P<0.01, Chi-squared test with Bonferroni correction, n = 90 animals per genotype summed across three separate experiments). (I) SNG-1::ARGO in the DA9 neuron imaged with Super Resolution spinning disk confocal microscopy with deconvolution. Area inside dashed white line contains autofluorescence from the intestine. Teal dashed oval encircles the neuron cell body; teal arrowhead points to the most proximal presynapse. Note that transport packets containing SNG-1::ARGO are visible throughout the axon between the cell body and the proximal synapse. Scale = 5 um. (Ii-ii) Transport packets with brighter RFP vs GFP fluorescence are indicated with orange arrows. Scale = 1 um.

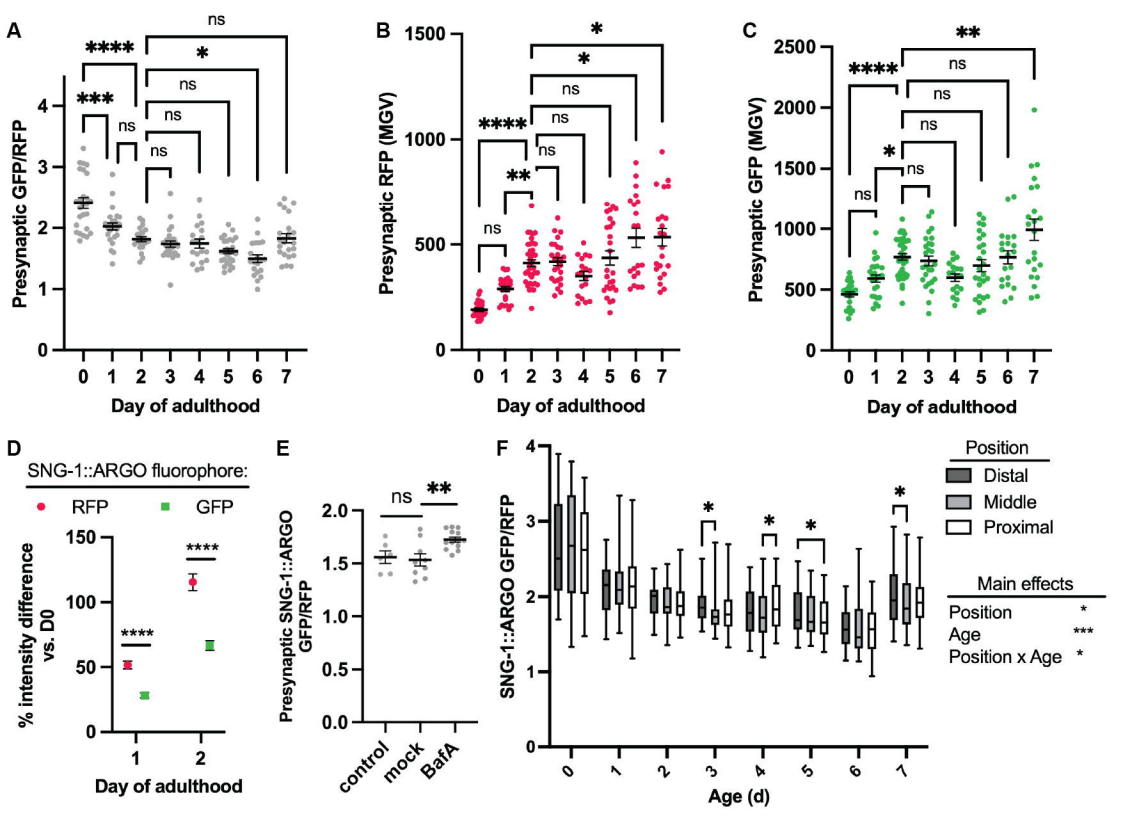

Figure 2. Presynaptic SNG-1::ARGO shows a decline in steady-state GFP/RFP fluorescence, indicative of accumulation within acidic compartments, during early adulthood in the DA9 neuron. (A-C) Average presynaptic RFP/GFP ratio (A), and the underlying intensity data for RFP (B) and GFP (C) from SNG-1::ARGO. Data points are each the mean of all presynapses from a single neuron. Here and elsewhere unless otherwise noted, mean ± SEM are plotted. (D) Percent change in average presynaptic RFP and GFP intensity from Day 0 (A0) through Day 2 (A2) of adulthood, calculated from the data in B-C. (E) Presynaptic SNG-1:ARGO GFP/RFP in A3 animals injected with Bafilomycin A (BafA), vehicle ("mock"), or uninjected ("control"), quantified and displayed as in A. (F) SNG-1::ARGO presynaptic GFP/RFP by presynapse position along the axon. ns: not significant, *P<0.05, **P<0.01, ***P<0.001, ****P<0.0001, one-way ANOVA (A-C,E) or two-way ANOVA (D,F) with Tukey post-test.

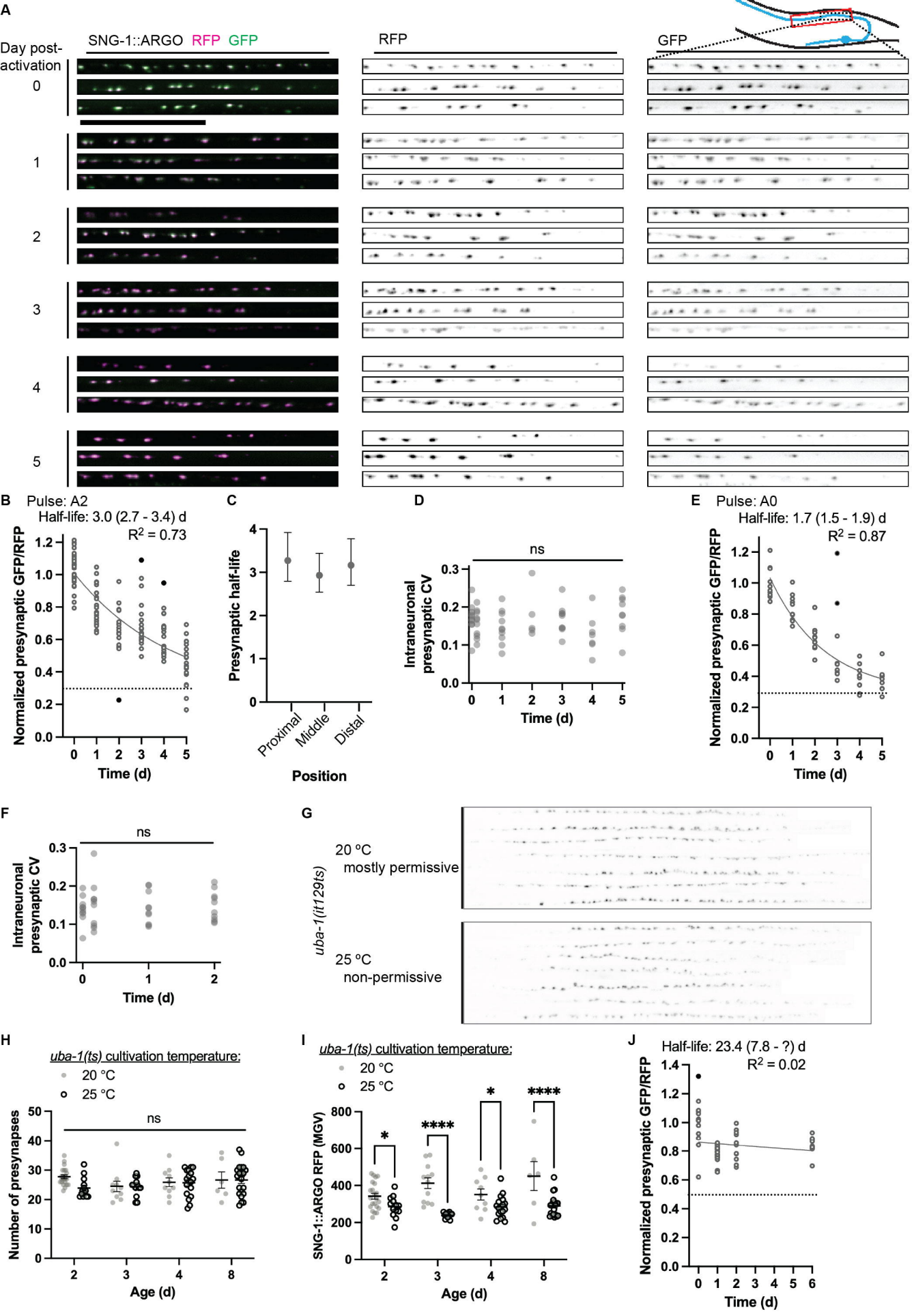

Figure 3. Quantification of SNG-1::ARGO turnover in the DA9 neuron. (A-B) Example images (A) and quantification (B) of SNG-1::ARGO in DA9 presynapses from turnover experiment with the pulse at A2. (A) Proximal synapses from three animals per time-point (different cohorts of animals are imaged at each timepoint). Scale = 30 µm. (B) One-phase exponential decay function fit to SNG-1::ARGO turnover data with the pulse at A2; each data point shows the average presynaptic SNG-1::ARGO GFP/RFP ratio from all the presynaptic puncta in a single neuron. Dashed black line shows the experimentally calculated background, which comes from autofluorescence. Outlier data points that were excluded from the curve calculation are shown in black. (C) SNG-1::ARGO presynaptic half-life by proximal-distal position relative to the neuron cell body (mean ± 95% C.I.). (D) The average coefficient of variation (CV) for all the presynaptic puncta within each neuron does not change at any chase timepoint compared to the pulse, suggestive that there is effectively a uniform SNG-1::ARGO turnover rate across all presynapses within one neuron. (E-F) From a turnover experiment with the pulse at A0, one-phase exponential decay function (E) and intraneuronal variance between synapses (F). (G-I) The *uba-1(it129ts)* mutant at the non-permissive temperature, 25 C, shows no obvious defect in presynapse localization (G) or number (H) but reduced abundance of SNG-1::ARGO at each presynapse (I). Two-way ANOVA with Tukey post-test. (J-K) A turnover experiment started at adult Day 2 indicates that the SNG-1::ARGO presynaptic turnover is slowed in the *uba-1(it129ts)* mutant (J).

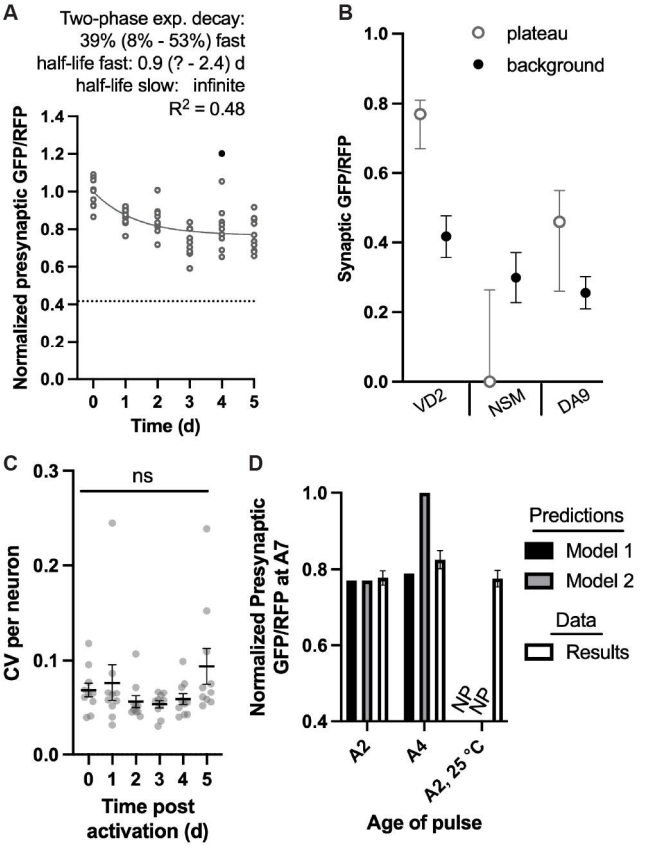

Figure 4. Biphasic SNG-1::ARGO turnover in the VD2 neuron. (A) SNG-1::ARGO turnover experiment in the VD2 neuron with the pulse at A2. Best-fit parameters and curve for a two-phase exponential decay function are shown, as this model was significantly favored over a one-phase exponential decay. (B) Comparison of the one-phase exponential decay function plateau (best-fit value and 95% C.I.) versus the background calculated from the images (mean ± 95% C.I.) for each neuron identity with the pulse at A2. Data are from the experiments shown in 5A (VD2), S2I (NSM), and 3B (DA9). (C) Intraneuronal variance between individual presynaptic puncta during the VD2 turnover experiment. Each data point shows the CV for all the presynaptic puncta from one neuron. (D) Predicted presynaptic GFP/RFP values from the two models, qualitatively compared to results from a separate experiment in which animals with VD2 neuron SNG-1::ARGO were pulsed at different ages/conditions and imaged at A7. NP: no prediction.

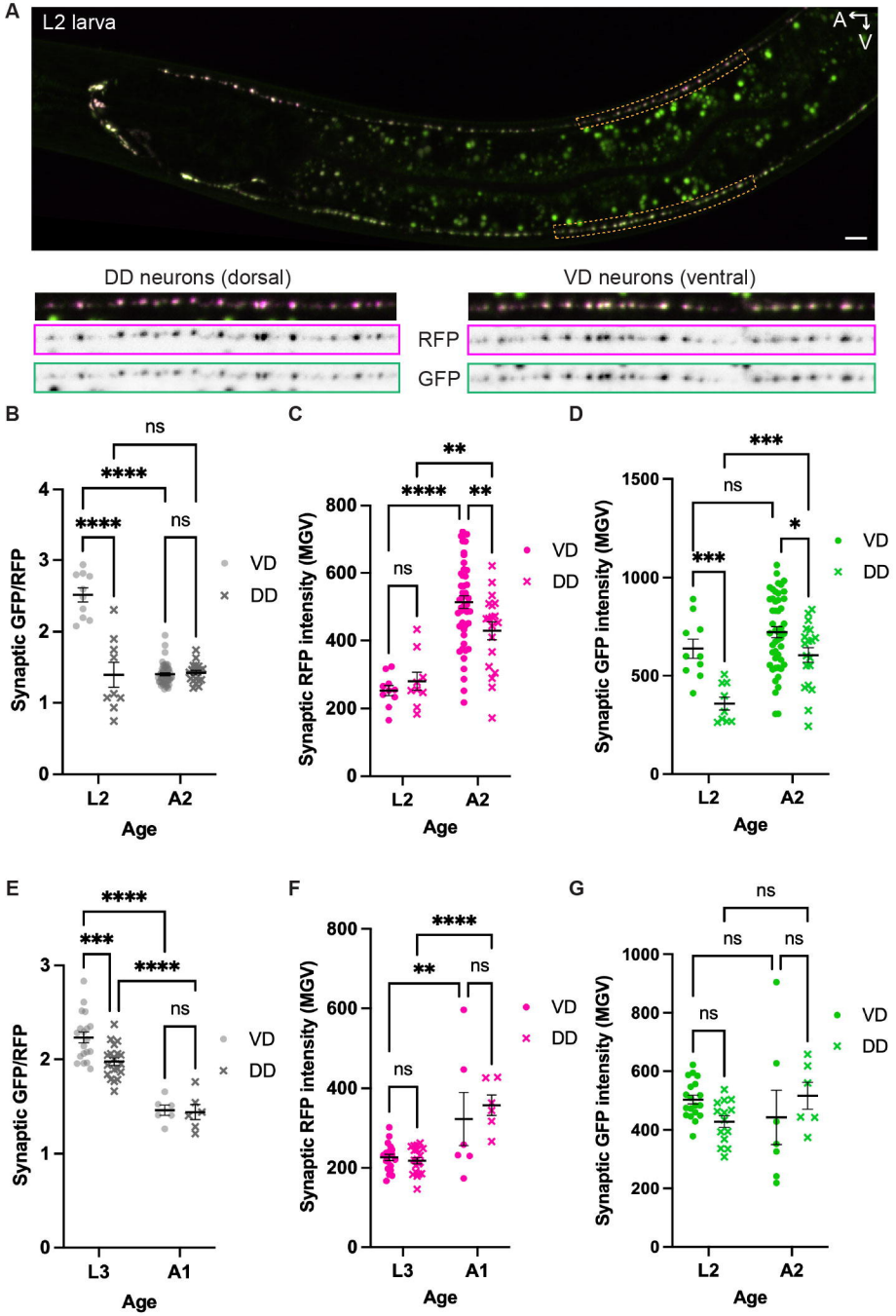

Figure 5. SNG-1::ARGO steady-state GFP/RFP ratio is low in the newly remodeled DD presynapses. (A) Representative image of SNG-1::ARGO in a L2 larva, in which a lower GFP/RFP ratio in the DD neurons compared to the VD neurons is apparent. (B-G) Comparison of presynaptic SNG-1::ARGO GFP/RFP ratio (B,E) and raw fluorescence intensities (C-D,F-G) in the VD versus DD neurons shows a difference at L2 that is abolished by adulthood. Note that the DD ratio at the L2 versus A2 ages is similar (B), whereas the DD ratio at L3 is higher than at A1 (E). Two-way ANOVA with uncorrected Fisher's LSD, with single pooled variance.

Table 1. Specificity and Efficacy of SNG-1::ARGO Activation by Heat-shock-Promoter driving *Cre* recombinase.

Specificity		
Neuron	**Age scored (d of adulthood)**	**GFP not recombined without heat shock (n)**
DA9	>= 4	95% (146)
NSM	>=6	100% (43)
VD2	>=5	99% (88)
Efficacy		
Neuron	**Age heat-shocked (d of adulthood)**	**GFP recombined after heat-shock (n)**
DA9	0	97.3% (108)
DA9	2	94% (65)
NSM	2	100% (55)
VD2	2	97% (38)

Parameters were assessed in strains carrying *sng-1(syb3140car2[argo])* for DA9 and NSM and *sng-1(syb3140[unstable argo])* for VD2. All strains carried an individual neuron-specific flippase (one per strain), and an integrated transgene composed of heat-shock promoter driving *Cre* recombinase (*heSi160*). Specificity means how often the *GFP* was not excised in the absence of heat-shock, and Efficacy means how often the *GFP* was excised upon heat-shock of 1 h at 34 ºC.